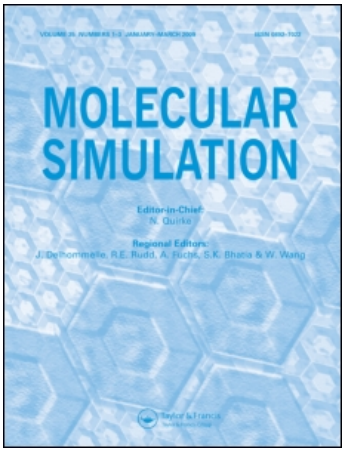


**Molecular Simulation**
Publication details, including instructions for authors and subscription information:
http://www.informaworld.com/smpp/title~content=t713644482

# Nanoscopic modeling of a carbon nanotube force-measuring biosensor

C. Roman[a]; F. Ciontu[a]; B. Courtois[a]
[a] TIMA Laboratory, Grenoble, France

**To cite this Article** Roman, C. , Ciontu, F. and Courtois, B.(2005) 'Nanoscopic modeling of a carbon nanotube force-measuring biosensor', Molecular Simulation, 31: 2, 123 — 133
**To link to this Article: DOI:** 10.1080/08927020412331308511
**URL:** http://dx.doi.org/10.1080/08927020412331308511

*Molecular Simulation*, Vol. 31, No. 2–3, 15 February–15 March 2005, 123–133



# Nanoscopic modeling of a carbon nanotube force-measuring biosensor

C. ROMAN*, F. CIONTU and B. COURTOIS

TIMA Laboratory, 46. Av. Félix Viallet, 38031 Grenoble, France

*(Received March 2004; in final form April 2004)*

In this paper we perform a theoretical study of a potential design of a carbon nanotube device able to transduce forces developed at the scale of basic cellular processes into electric current variations. The first part of this study consists of an assessment of the sensitivity of the device with forces in the tens of pico Newtons (pN), developed typically at the cellular scale. In the second stage, we focus on the transduction of the deflection of a cantilever into an electrical signal, employing methods borrowed from non-equilibrium Green's functions. Several issues related to the importance of thermal effects in the proper operation of the sensor are then discussed. Following a simple method we include non-zero temperature through molecular dynamics in quantum conductance calculations that results in the displacement-current characteristic found at the end of this paper.

*Keywords*: Carbon nanotubes; Nano-mechanical cantilever; Biosensors; Molecular modeling; Multi-terminal conductance



## 1. Introduction

The last years have brought nanotech applications closer to reality mainly due to considerable progress in fabricating nanostructures with controlled properties. Carbon nanotubes followed this path with huge advances in synthesis techniques as well as functionalization [1], solubility [2] and selection [3]. Given this trend it is reasonable to extrapolate that in several years it will be possible to have nanotubes with well-controlled properties at significantly lower costs. Aside from this, an essential aspect that allows envisioning the design of carbon nanotube based structures is the very good agreement between theoretical models and experimental data.

Bio-sensing is one domain offering clear opportunities to transpose theoretical and technological advances related to nanotubes into applications. In this paper we investigate theoretically a potential design of a carbon nanotube sensor able to transduce forces developed at the scale of basic cellular processes into electric current variations, although measuring cell forces [4] is just one possible application for this device.

Several papers have reported the conversion of bio-molecular processes into micro-cantilever deflections [5,6]. Furthermore, mass measurements in the femto-gram range were achieved using carbon nanotube-based cantilevers [7]. Compared to the former, carbon nanotube devices would have the advantage of a far better scale compatibility with elementary biological processes. This scale compatibility comes as the first of four requirements for future generation biosensors as identified in Ref. [8], followed by label-free detection, scalability in view of massive parallelization and wide dynamic range.

The reminder of the paper is organized as follows. In Section 2 we explain the operation principle of the sensor. Section 3 contains the calculation details performed to characterize the mechanics of the sensor, while the transduction of mechanical movement into a current variation is covered in Section 4. The quantum conductance computation procedure is separately described in the Appendix in order to keep the presentation flow as fluent as possible. Finally, we present our conclusions and discuss future work and possible improvements.

## 2. Operation principle

The proposed sensor, sketched in figure 1, transduces the deflection of a carbon nanotube, upon the application of

*Corresponding author. Tel.: +33-476-574-834. Fax: +33-476-473-814. E-mail: cosmin.roman@imag.fr

*Molecular Simulation*
ISSN 0892-7022 print/ISSN 1029-0435 online © 2005 Taylor & Francis Group Ltd
http://www.tandf.co.uk/journals
DOI: 10.1080/08927020412331308511

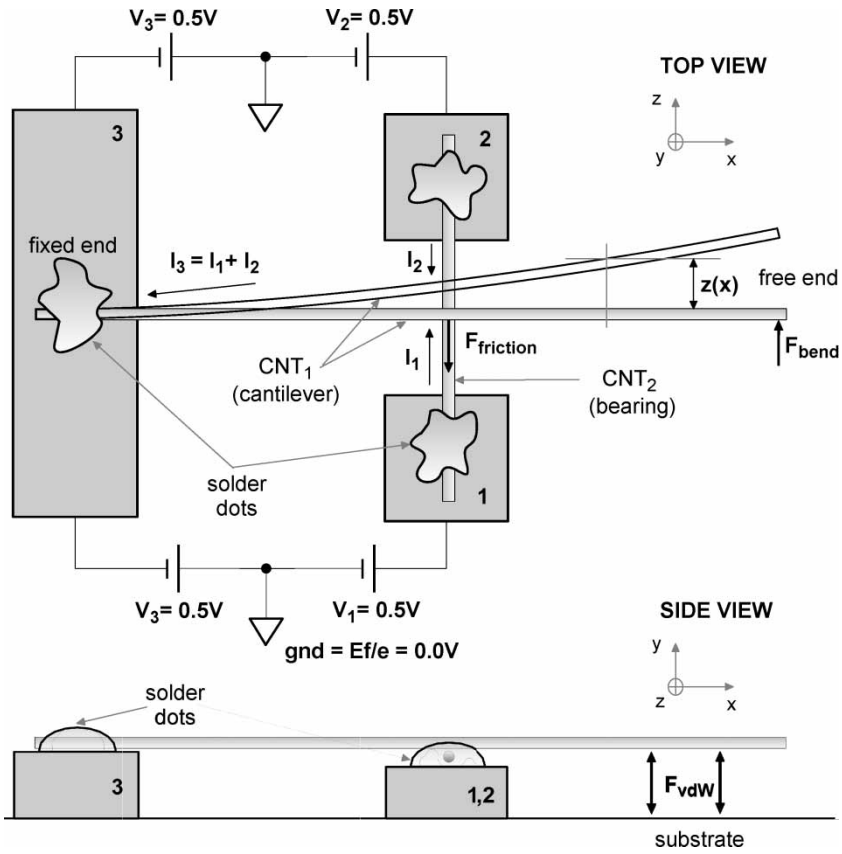


Figure 1. Schematic representation of the operation principle of a carbon nanotube-based force-measuring sensor, including electronic biasing.



an external force, into an electric current difference at the ends of a second nanotube, perpendicular to the former.

Three of the four nanotube ends are fixed to metal leads and one is free to move, being the end to which an external force will be applied. Mechanically, one tube is a cantilever while the other one is a linear bearing. The bearing is placed underneath the cantilever, restraining its vertical movement and preventing it from bending and sticking to the substrate. As it will be shown in Section 3, the inter-tube friction will not impede the cantilever from bending laterally under an external force, although it will modify the amplitude of thermal fluctuations in the region of the junction.

Apart from mechanical stability, the three metallic leads provide a means to electrically bias the device. In this paper we adopt a simple DC biasing scheme with the two terminals of the bearing set to $+$V, and the single terminal of the cantilever set to $-$V. In the steady-state, when no external force is applied upon the cantilever, the currents flowing through the two branches of the bearing should be approximately equal, even if in practice there will always be an offset owing to unequal branch-length or differences in the doping of the branches. However, if an external force is applied, the cantilever will bend elastically, modifying the length and consequently the current ratio of the two branches. Length-scaling of the conductance is impossible in a ballistic tube, which means that the bearing should be previously doped with impurity atoms. Thus by measuring the current imbalance resulting at the two terminals of the bearing, the cantilever's deflection can be obtained. The external force can be derived by multiplying the spring constant of the system with the previously determined deflection.

The junction's integrity is maintained mainly by van der Waals forces and additionally by hydrophobic–hydrophilic effects if the system is placed in water. However, a positive off-plane force, i.e. along $y$-axis, could compromise the weak junction formed between the tubes. This undesirable effect can be tackled either by confining the applied force in the $x$–$z$ plane or by stacking the tubes together with a third one in a bearing-lever-bearing sequence. Yet we will not address this issue in this paper and leave it for future work.

Basically the sensor is a molecular potentiometer whose actuation could be performed for instance by cell motility or by any other molecular phenomena. Even though it performs the same task as a lateral force microscope this sensor has the advantage of being embeddable, allowing the fabrication of sensor arrays that could measure force fields and not just individual forces.

## 3. Mechanics

The mechanical behavior of the device was captured at the level of molecular mechanics using a classical force field

which required an additional *ab initio* parameterization in order to cope with the heterogeneity of a system containing both carbon nanotubes and organic molecules. The cantilever-bearing complex has been studied under perturbations induced by forces of tens of pico Newtons (pN), forces comparable with those developed by cells during motility related processes.

A common choice for the mechanical modeling of carbon nanotubes is the Euler–Bernoulli beam theory, due to the essentially one-dimensional nature of carbon nanotubes. Previous studies on carbon nanotube-based AFM tips [9,10], nanotweezers [11], electro-mechanical resonators [7] and nano-switches [12] proved the validity of this theory even at the molecular level. However, above a certain threshold, stress induces buckling in nanotubes, usually accompanied by $sp^2$–$sp^3$ mixing. Moreover, atomic-like fluctuations of the van der Waals potential coupled with the position-dependent shape of the cross-junction, yield pseudorandom friction forces. These phenomena can hardly be taken into account by a continuous level theory, although attempts have been made with shell theories extended by homogeneous van der Waals potentials [13,14].

A better choice for modeling nanotubes in such complex situations is molecular dynamics. Carbon nanotubes were studied intensively using various force fields ranging from *ab initio* [15], tight-binding [16], Tersoff-Brenner [17] to very simple ones like CHARMM [18]. We adopted the last type as implemented in the freely available program NAMD [19]. This force field is faster than *ab initio* and semi-empirical methods allowing simulations with more than $10^6$ atoms for a few nanoseconds. Compared with the Brenner potential, that was successful in describing carbon–carbon interactions, the CHARMM force field was parameterized for a large spectrum of organic molecules, notably for amino acids and phospholipids [20]. This advantage becomes obvious when simulating the sensor, or just part of it, in contact with a cellular membrane.

### *3.1* Ab initio *force field parameterization*

Empirical force fields in CHARMM's class were previously employed in modeling carbon nanotubes [18,21] but their main focus was on hydrophobic–hydrophilic effects and not on the mechanics of large deformations in nanotubes. Accurate experimental information about Young's modulus and Poisson's ratio of carbon nanotubes is still missing from literature [22], constraining the parameterization procedures to rely on *ab initio* calculations. All quantum mechanical computations presented throughout this paper were performed with Siesta [23], within the density functional theory (DFT).

$$\begin{aligned} E_{\text{total}} &= (E_{\text{bond}} + E_{\text{angle}} + E_{\text{UB}} + E_{\text{dihed/imprp}}) + (E_{\text{vdW}} + E_{\text{elec}}) \\ &= \sum_{i\neq j} k_{ij}(|r_{ij}| - r_{0ij})^2 + \sum_{i\neq j\neq k} k_{\theta ijk}(\theta_{ijk} - \theta_{0ijk})^2 \\ &\quad + \sum_{i\neq j\neq k} k_{\text{UB}ij}(|r_{ik}| - r_{0\text{UB}ik})^2 \\ &\quad + \sum_{i\neq j\neq k} k_{\phi ijkl}(1 + \cos(n\phi + \delta)) \\ &\quad + \sum_{i\neq j}\left(\frac{A}{|r_{ij}|^{12}} - \frac{B}{|r_{ij}|^6}\right) + \sum_{i\neq j} \varepsilon_{14}\frac{Cq_iq_j}{\varepsilon_0|r_{ij}|} \end{aligned} \quad (1)$$

The first set of simulations were conducted in order to obtain statistics on bond lengths, angles, Urey-Bradley (UB) and improper dihedrals values as required by CHARMM, formally defined by equation (1). In this equation the first bracket delimits the energy contribution of the bonded atoms while the second bracket corresponds to non-bonded atoms. This was achieved for three different nanotubes, one armchair (5,5), one zig-zag (8,0) and one chiral (6,3) having approximately the same features. The nanotubes, considered infinitely long, were relaxed in a variable-cell until residual forces dropped under 0.01 eV/A. We used a LDA Hamiltonian, an integration grid cut-off of 60 Ry, a double zeta (DZ) atomic orbital basis set with an energy shift of 160 meV or equivalently a confinement/cut-off radius of 2.85 Å. The results are summarized in table 1.

Generally there are three inequivalent bonds for chiral nanotubes, while armchair and zig-zag tubes have only two. This as well yields three inequivalent angles and UBs, and nine inequivalent improper dihedrals. The improper dihedrals histogram revealed that there is no unique equilibrium value, leading to the exclusion of this term from the total energy. The final values for $r_0$, $\theta_0$, $r_{0\text{UB}}$ and $R_{\text{vdW}}$ are presented in table 2.

The second phase of the parameterization procedure consisted in fitting the spring constants $k$, $k_\theta$, $k_{\text{UB}}$ and the Lennard–Jones well-depth $\varepsilon_{\text{vdW}}$ against energy versus

Table 1. Mean bond length, angles and Urey-Bradley terms.

| CNT type | | (5,5) Mean | (8,0) Mean | (6,3) Mean |
|---|---|---|---|---|
| Bond (Å) | A | 1.430 | 1.438 | 1.434 |
| | B | 1.434 | 1.438 | 1.426 |
| | C | 1.434 | 1.431 | 1.442 |
| Angle (deg) | AB | 118.640 | 116.789 | 119.614 |
| | AC | 118.645 | 119.719 | 119.239 |
| | BC | 119.460 | 119.719 | 117.305 |
| UB (Å) | AB | 2.463 | 2.449 | 2.472 |
| | AC | 2.463 | 2.481 | 2.482 |
| | BC | 2.476 | 2.481 | 2.450 |
| Improper (deg) | | 84.004 | 87.191 | 84.954 |

Table 2. CHARMM force-field parameters.

| | | | |
|---|---|---|---|
| $k$ | 189.581 (kcal/mole/Å$^2$) | $r_0$ | 1.433 (Å) |
| $k_\theta$ | 115.724 (kcal/mole/deg$^2$) | $\theta_0$ | 118.892 (deg) |
| $k_{\text{UB}}$ | 22.699 (kcal/mole/Å$^2$) | $r_{0\text{UB}}$ | 2.467 (Å) |
| Intra-tube | | | |
| $\varepsilon_{\text{vdW}}$ | −0.105 (kcal/mole) | $R_{\text{vdW}}$ | 4.000 (Å) |
| Inter-tube | | | |
| $\varepsilon_{\text{vdW}}$ | −0.70 (kcal/mole) | $R_{\text{vdW}}/2$ | 1.992 (Å) |

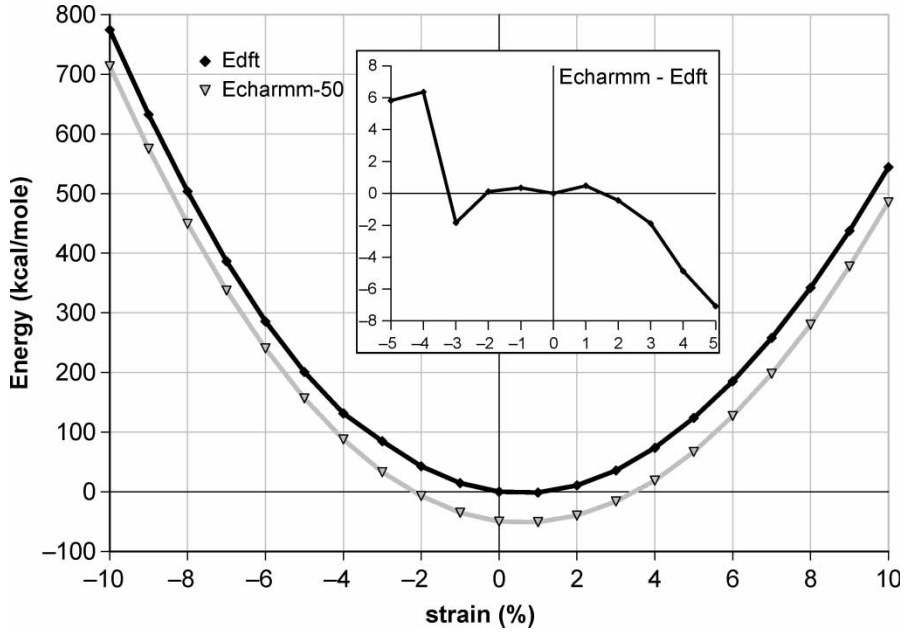


Figure 2. Energy-strain characteristics as obtained with SIESTA (DFT) and NAMD (CHARMM), respectively. The inset details the error around origin (the curves were shifted for better visualization).



strain curves as obtained with Siesta. Since our calculations are similar with those performed in Ref. [15] and rely on the same code, we took into account their calculated Poisson's ratio of 0.14 when preparing pre-strained tubes for relaxation. As opposed to the same reference we extended the study to strains in the range $[-10,10]\%$ with a step of 1%, in order to obtain well-behaved parameters even at large deformations. The system under study was a (5, 5), 5 cells long carbon nanotube. To accelerate the forthcoming relaxation, for each strain we took the already relaxed tube and modified its length to $l_0(1 + \Delta l/l_0)$ and radius to $r_0(1 - \nu\Delta l/l_0)$. A full energy minimization was again performed, but not before constraining the boundary atoms in planes perpendicular to the tube's axis.

In order to maintain physical relevant quantities like positive spring constants and a negative Lennard–Jones well-depth we used Lagrange multipliers within the goal function. Figure 2 shows the comparative energy-strain curves, where the one corresponding to CHARMM was obtained using the optimized force field parameters summarized in table 2; these parameters were used in every molecular dynamics simulation throughout the remainder of this paper. A closer look at the same figure reveals that the DFT curve is asymmetric with respect to zero strain and is especially noticeable at large strains. In order to include this anharmonic behavior we had to add an intra-tube Lennard–Jones potential term that has different parameters from the inter-tube one.

### *3.2 Mechanical characteristics*

In the first MD simulation, the cantilever measuring 36 nm was pushed upon with a constant force of 10 pN equally distributed between its ten terminal atoms while keeping fixed the other end of the tube.

Turning on the force at the initial simulation time was equivalent with applying a broad-band step function stimulus, exciting all the frequency modes of the system simultaneously. Because it lacked any friction or dissipation, the cantilever could have oscillated indefinitely. Nevertheless this impulse response type of simulation contains a lot of information about the mechanical properties of the system. For instance the continuous component of the spectrum gives the final displacement as would be obtained in the presence of dissipation.

Three different positions of the (5,5) bearing tube, measuring 20 nm, were chosen to study the influence of the friction; at one third, at half and at two thirds from either edge of the cantilever. Relaxation under van der Waals forces was performed before performing any dynamics, resulting in the formation of the non-covalent junction between the tubes. As before the simulation step of the molecular dynamics was of 1 fs and the total simulation time was of 0.5 ns. This time interval proved to be sufficient in capturing at least one period of the cantilever's fundamental mode [see figure 3 especially (a) and (b)].

Except for inter-tube van der Waals interaction, there should be in principle no deflection along $y$ since the applied force is constrained in the $x$–$z$ plane. However, figure 4 reveals a different situation. Even if initially at constant height, the cantilever's tip starts to oscillate with increasing amplitude, a closer examination confirmed that the motion of the cantilever is stick- and slip-like due to rapid fluctuations of the van der Waals potential of the underlying tube. As we will see in the next section, this spurious movement will greatly influence the charge

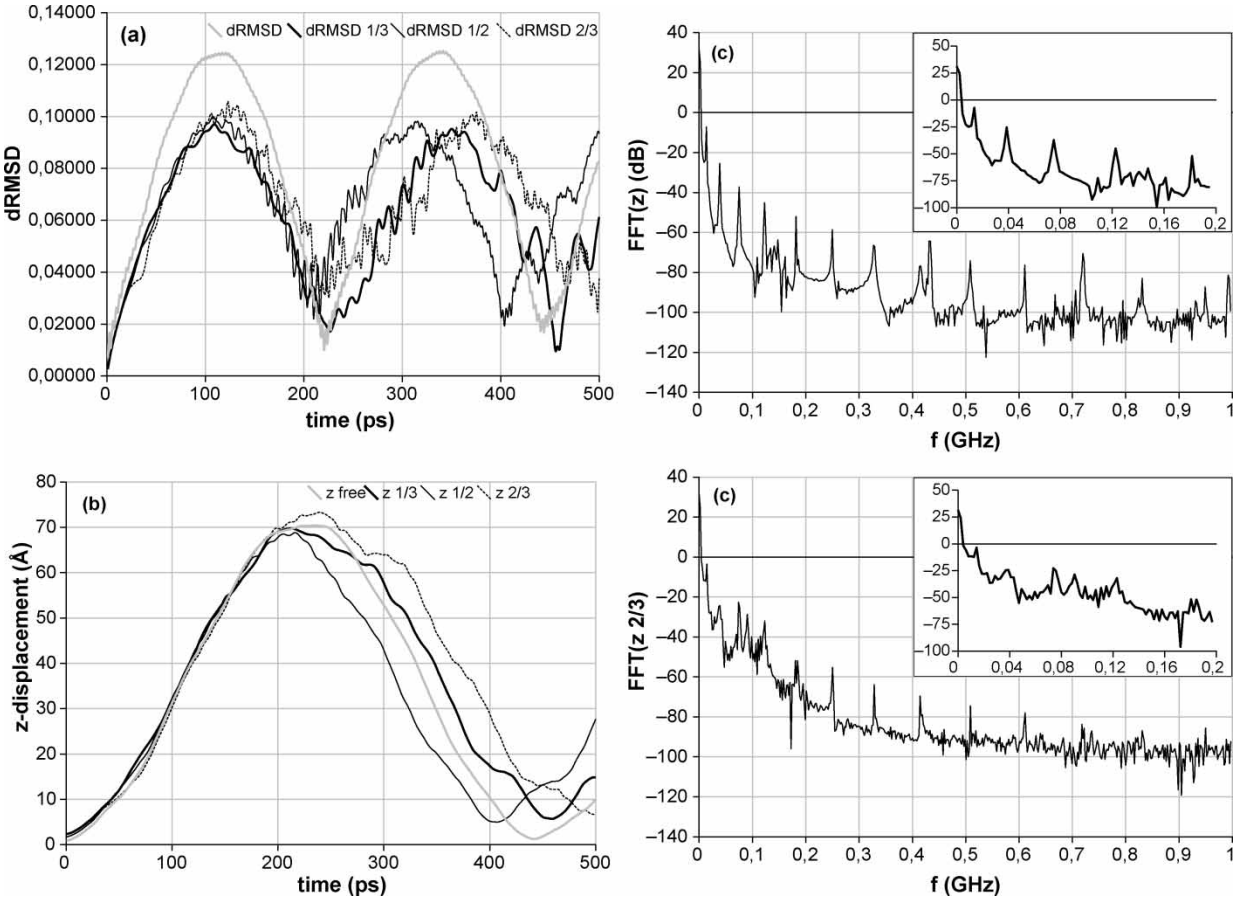


Figure 3. Different curves relevant to the mechanical behavior of the system (a) Differential RMSD of all atoms of the cantilever; (b) Cantilever's deflection along $z$-axis (from one atom found on the tip); (c) FFT of the $z$-displacement showing the influence of the thermal noise (see text for details).



transport through the junction as the latter is extremely sensitive to the inter-tube distance.

As opposed to the free cantilever case, the bearing presence adds friction. The mechanical work that is done to move the cantilever against friction, transforms to heat as it can be observed in showing the differential RMSD. Heating phenomenon can be also observed in the frequency domain by noticing in figure 3(c) the noise added and resonance smearing in cantilever-bearing case as opposed to the free cantilever case. We plan further studies of this system in the presence of a thermostat capable of draining out the heat produced by friction.

## 4. Electronic transport

The transduction of the cantilever deflection into an electrical signal has been investigated within the Landauer–Büttiker formalism. We considered only the $\pi$ band electrons as being relevant for the conduction and use a tight-binding Hamiltonian. Thermally fluctuating ion positions were obtained from an underlying molecular dynamics simulation at room temperature.

Modeling the charge transport through carbon nanotube cross-junctions is delicate. Even though accurate DFT-level computation of carbon nanotube cross-junctions were previously achieved [24], we had to consider a simplified tight-binding description of the electrons, mainly because of the system's size. Moreover, a current imbalance at the two terminals of the bearing is expected only when its conductance scales in the two branches with length, forcing a clear delimitation of the bearing from the leads, along with the need to include the leads in the overall system.

At zero temperature, junction tunneling would be phase-coherent. However, the zero temperature assumption is not practical, since this sensor is bound to operate at room temperature. As already explained the junction is relatively free to move in the $x-z$ plane being confined only vertically by non-covalent bonding. Under thermal fluctuations the position of the junction will act as a phase-breaking scatterer. In fact we count on this effect to obtain the non-zero temperature behavior of this device, and argue that at zero temperature the sensing mechanism can be non-monotonic being thus of no practical importance.

### *4.1 Method description*

The scheme involved in quantum transport simulations is similar with the one described in Ref. [25]. However, we

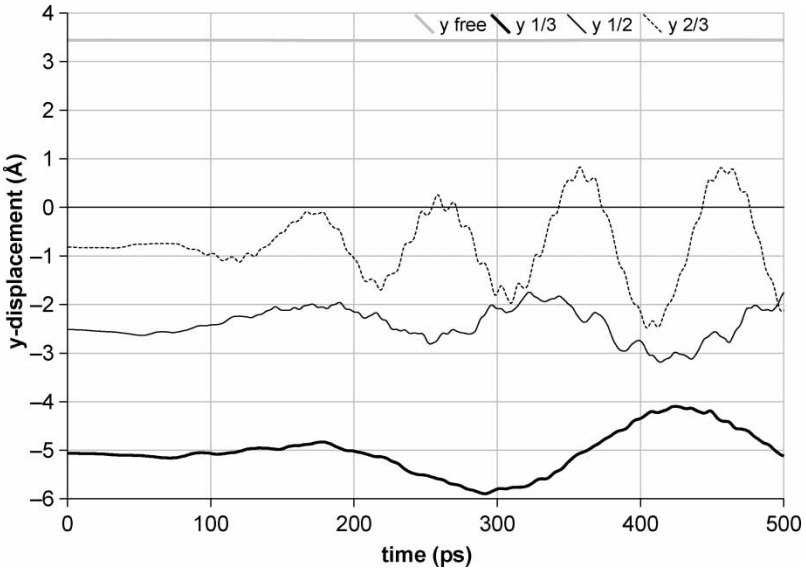


Figure 4. Cantilever's deflection along the ordinate for the free cantilever case and for other three positions of the bearing. The oscillations appear as a consequence of friction-induced heating as explained in the text.



had to modify this technique to include multi-terminal conductance calculations in the presence of tunneling through a non-covalent junction. We used the tight-binding Hamiltonian [27] detailed in equation (2) including only $\pi$ orbitals, but as opposed to typical calculations we included the cosine factor reminiscent from Slater–Koster's TB scheme that accounts for the anisotropic inter-tube coupling. An exponential decay was also considered to limit the interaction range between non-covalently bonded atoms of the two distinct tubes. The first bracket in the Hamiltonian delimits intra-tube sites and hopping while the second describes inter-tube interaction.

$$H = \left( \sum_i (\varepsilon_{0i} + \delta\varepsilon_{0i} - |e|V(r_i)) c_i^\dagger c_i + \sum_{(i \neq j)} t_{0ij} \exp\left(\frac{a_{C-C} - r_{ij}}{d}\right) c_i^\dagger c_j \right) + \left( \sum_{(i \neq j)} \tau_{0ij} \cos(\theta ij) \exp\left(\frac{a_{g-g} - r_{ij}}{\delta}\right) c_i^\dagger c_j \right) \quad (2)$$

The voltage biasing of the system corresponds to figure 1, and was chosen in this way to emphasize the length difference of the two branches. Any other scheme involving a voltage drop on the bearing would wash-out this effect since the intra-tube conductance is unquestionably higher than the inter-tube one.

A controversial issue might be the potential profile we adopted in this study. The cantilever can be considered in equilibrium with its lead and thus we considered that the potential on this tube is uniform and equal to $-$V. The same was considered for the bearing, i.e. having a constant potential, even though it contained doping atoms that could prevent an effective screening of the local potential induced by the cantilever, especially in the region of the junction. We believe that a charge self-consistent tight-binding method could clarify this issue and leave it for future studies.

The central quantity in the Landauer–Büttiker formalism is the transmission matrix which can be calculated, using the Fisher–Lee relation, from the Green's functions of the system. To accelerate the computation of the Green's functions we partitioned the system as in figure 5. Pristine, infinite (5,5) CNTs were placed at the end of each of the first three domains (denoted with $H_{1\ldots3}$) of the sensor's tubes to simulate the effect of electron reservoirs, i.e. leads. The bearing tube was "doped" by modifying the on-site energy from $\varepsilon_0$ to a random value equally distributed in $[\varepsilon_0 - 1\,\text{eV}, \varepsilon_0 + 1\,\text{eV}]$ and denoted with $\delta\varepsilon_0$ in the Hamiltonian of equation (2). The leads along with the tubes they contact were set to an electrochemical potential of $\pm 0.5$ eV by shifting the on-site energy with $-|e|V \equiv \mu$.

After completing the Hamiltonian's matrix elements, a fast, self-energy-based elimination method that is described in Appendix was used to invert an otherwise large system matrix. Self-energies were propagated backwards from leads to junction as illustrated in figure 5. Practically just the junction Green's function was inverted because its Hamiltonian is not sparse as opposed to the other domains where the inter-tube interaction could be neglected. After computing the Green's functions and self-energies for the junction, the Fisher–Lee relation in conjunction with the Landauer–Büttiker formula allowed us to obtain the conductance functions: $G_{12}$, $G_{13}$ and $G_{23}$, which were further convoluted with the thermal smearing function to obtain the three currents $I_{1\ldots3}$.

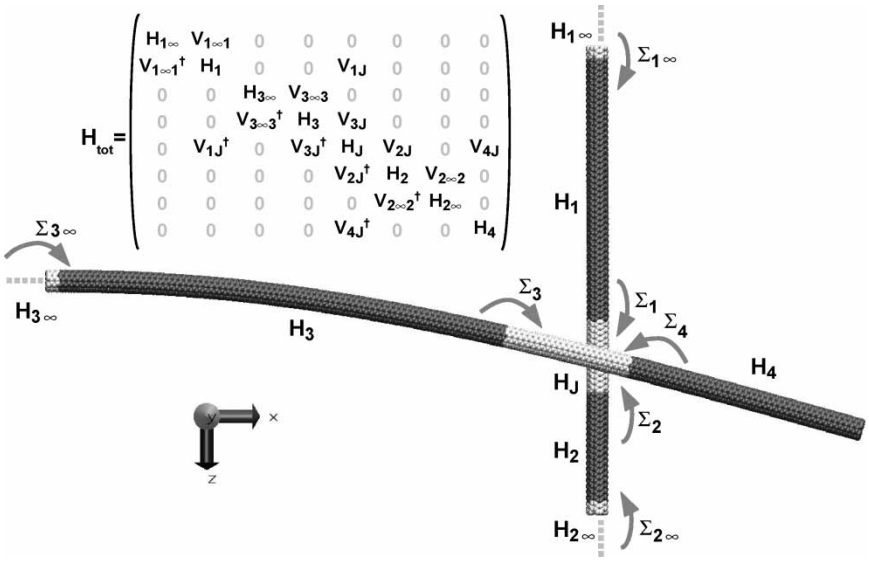


Figure 5. Real-space partitioning and Hamiltonian of the system.



### *4.2 Electrical characteristics*

Initial zero temperature simulations with the cantilever deflected in different positions proved the device to be non-monotonic. However, as counter-intuitive may appear, this is acceptable within quantum theory of electronic transport if one takes into account the short length of the two branches of the bearing. As they contain less than a few thousand atoms each, conductance fluctuation is possible, and this could be further enhanced by the sharp dopant distribution we used. Maybe even more important tends to be the atomic detail of the junction. Deflections as low as half an Angstrom give rise to important fluctuations in $G_{13}$ and $G_{23}$ as can be observed in figure 6, while $G_{12}$, seems to be insensitive in the same conditions.

The zero-temperature, non-monotonic sensing curve limits the operation of the device in the ambient temperature range, where thermal fluctuations can effectively break the phase-coherence of the charge carriers as we shall see in the following paragraphs. This temperature constraint is not even a bit upsetting since the sensor was imagined from the beginning to work in biocompatible conditions, of which ambient temperature (300 K) is one of the most important.

In view of taking into account thermal effects we took samples from the dynamical trajectory of the system as obtained in section 3. We did that instead of properly sampling the trajectory of a thermally fluctuating cantilever around each equilibrium deflection of interest, because the molecular dynamics relaxation of the sensor is very slow. This inconvenience is caused by the acoustic branch modes, of which the lowest frequency is somewhere at 2 GHz, or correspondingly having a period of 0.5 ns. However, we plan to work this out using a continuous shell theory to mechanically pre-condition the system by deflecting the cantilever to position close to equilibrium, and then relax through a heat-bath coupled molecular dynamics.

Around a given junction position we took other twenty five closely located sites. The length of the distribution interval was of $\sim 2$ Å, consistent with thermal displacement fluctuations as known from the classical cantilever theory. After computing the currents as described in Appendix the obtained values were convoluted with a thermal-smearing function yielding the curve in figure 7. This is actually a second smearing and it was considered here for phase-randomization of electrons tunneling through a mechanically fluctuating junction. This should not be confounded with the smearing applied to obtain the smooth conductance functions of figure 6, as this first smearing corresponds to the thermal broadening of the Fermi-Dirac distribution.

## 5. Conclusions

After investigating the carbon nanotube-based sensor proposed in section 2 by modeling phenomena characteristic to different scales, we evaluate positively its suitability for measuring forces specific to the cellular scale. We note, however, several challenges posed by the coupling of phenomena belonging to different scales like the influence of the inter-tubes distance, typically modeled though molecular dynamics, and the variation of the currents computed through the quantum transport method described in Appendix.

The benefits of such sensor lie in its reduced features, and integrated electronic read-in circuitry that would eliminate the need of massive and expensive laboratory sensing instruments. We do consider, however, that further

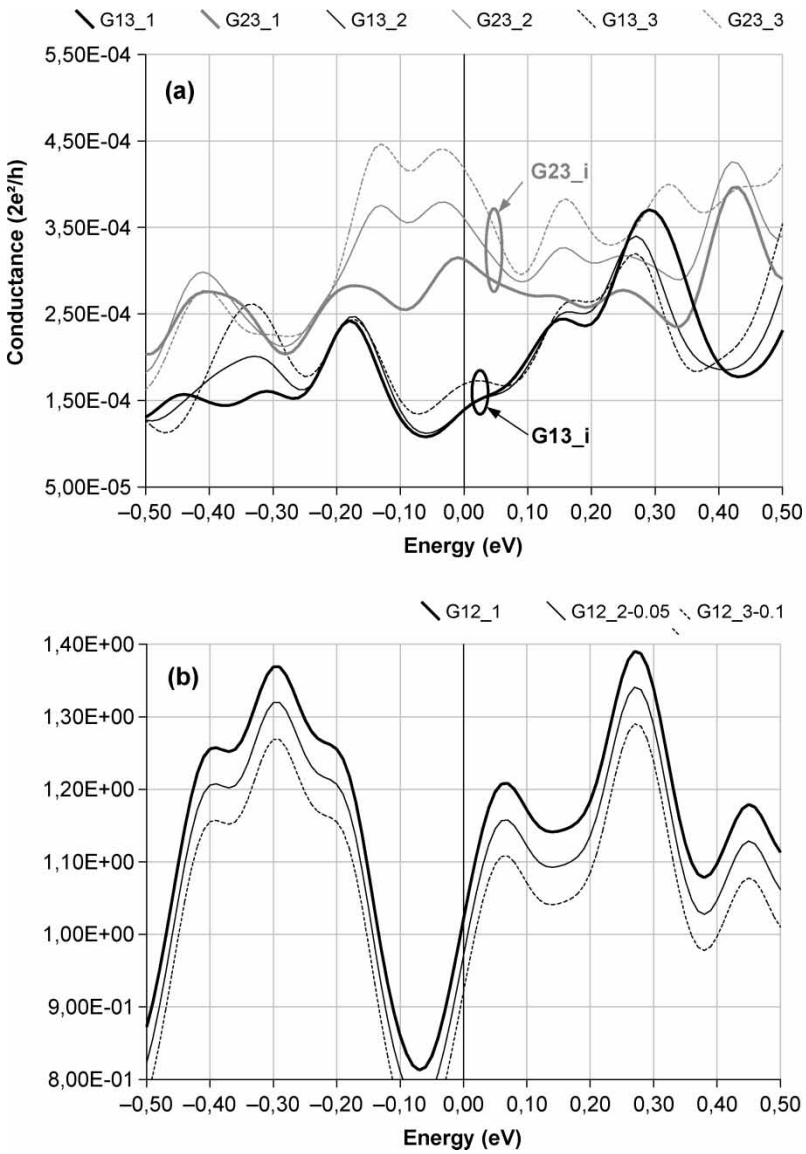


Figure 6. Smeared conductance functions. (a) Inter-tube varies strongly at small displacements of the cantilever; (b) Intra-tube conductance is insensitive with respect to cantilever's position (the curves were shifted for better visualization).

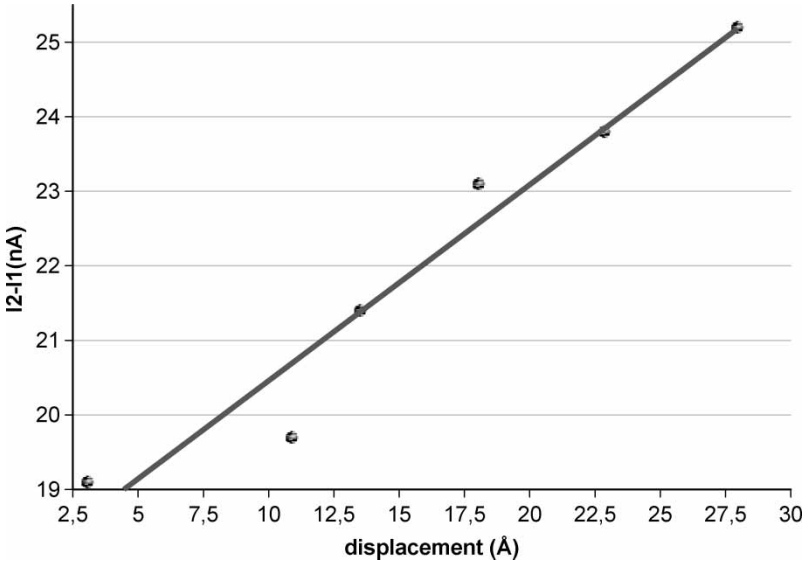


Figure 7. Overall current-deflection characteristic of the sensor plus the linear fitting line.

studies are required before any fabrication plans are made for this device. The primary goal of this paper was to prove rather qualitatively and not necessarily quantitatively that such a molecular force sensor is operational. Future work will have to take into account more thoroughly and systematically the influence of temperature on the operation of this device.

## Acknowledgements

The authors would like to thank Dr Stephan Roche for his help in elucidating the various aspects involved in modeling the quantum electronic transport. C. Roman would also like to acknowledge and thank Prof. Barbu Constantinescu for his useful comments and encouragements.

## Appendix

This Appendix details the quantum conductance calculation procedure, by first describing how the Green's functions corresponding to various domains of the real-space were calculated and then how the electrical currents were derived starting from the transmission matrix.

An important simplification is obtained by partitioning the Hamiltonian in several domains, as depicted in figure 5. Except for the junction every other domain is free of inter-tube interaction terms in the Hamiltonian. Thus the Hamiltonian of these domains is sparse making it possible to apply very fast matrix inversion algorithms. On the contrary, the junction's Hamiltonian has many non-zero terms corresponding to non-bonded interacting pairs, even though their number was reduced to only those pairs that fall within a given cut-off distance of 7 Å. This is why the Green's functions of the junction could be obtained only by direct inversion. However, it should be noted that the matrix to invert was compact with respect to the overall system's matrix and in consequence it did not dominate the computation time.

For non-junction domains, a further refinement that can accelerate the computation is to sub-partition the Hamiltonian by splitting it in units of 20 atoms (see figure A.1) and then identify the interactions between successive units. The Hamiltonian thus becomes block-tridiagonal and easily invertible through elimination methods. However, there is a difference between leads (domains $1\infty$ to $3\infty$) and the cantilever-bearing complex (domains 1 to 4), in that the Hamiltonian of the leads is a semi-infinite periodic matrix and a different procedure is needed to calculate its Green's functions.

The parameters used in the construction of the Hamiltonian and overlap matrix are listed in table 3. Orbital overlapping was considered in order to improve the calculation accuracy and also because it added no significant complexity, as the overlap matrix is very similar and practically constructed in parallel with the Hamiltonian, by plugging the value of 0.129 in those positions occupied by nearest-neighbors (or covalently bonded) atoms.

$$H=\begin{bmatrix} H_{1\infty} & V_{1\infty 1} & & & & & & \\ V_{1\infty 1}^{\dagger} & H_1 & & & V_{1J} & & & \\ & & H_{3\infty} & V_{3\infty 3} & & & & \\ & & V_{3\infty 3}^{\dagger} & H_3 & V_{3J} & & & \\ & V_{1J}^{\dagger} & & V_{3J}^{\dagger} & H_J & V_{2J} & & V_{4J} \\ & & & & V_{2J}^{\dagger} & H_2 & V_{2\infty 2} & \\ & & & & & V_{2\infty 2}^{\dagger} & H_{2\infty} & \\ & & & & V_{4J}^{\dagger} & & & H_4 \end{bmatrix} \quad (3)$$

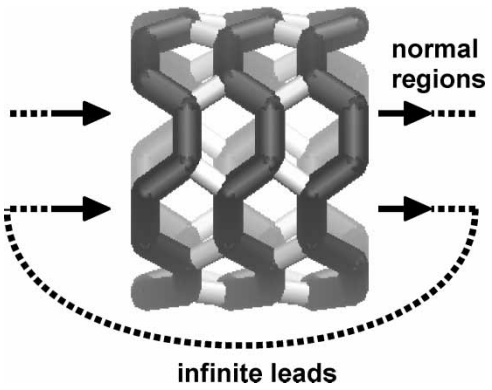


Figure A.1. Real-space sub-partition of the Hamiltonian in rings of 20 atoms (black). In the nearest-neighbor TB technique bonds correspond to hopping integrals. The white bonds represent interactions between rings.

The coarse-partitioned Hamiltonian looks like in equations (3) where **V** matrices represent interactions between domains. By convention all the omitted elements are zero. The overlap matrix has the same pattern as $H$. Further, let $K$ denote the inverse of the retarded Green's function. It follows that $K$ has the same pattern as $H$, i.e.

Table 3. Tight-binding Hamiltonian parameters.

| | | | |
|---|---|---|---|
| $\varepsilon_0$ ($\equiv E_F$) | 0 (eV) | d | 2 (Å) |
| $\delta\varepsilon_0$ | 1 (eV) | $\tau_0$ | −0.346 (eV) |
| $\mu_1=\mu_2=-\mu_3$ | −0.5 (eV) | $a_{g-g}$ | 3.35 (Å) |
| $t_0$ | −2.77 (eV) | $\delta$ | 0.45 (Å) |
| $a_{C-C}$ | 1.43 (Å) | $s_0$ | 0.129 |

$$K \triangleq (\varepsilon S - H) \equiv (G^{(r)})^{-1}$$

$$= \begin{bmatrix} K_{1\infty} & \tau_{1\infty 1} & & & & & & \\ \tau_{1\infty 1}^{\dagger} & K_1 & & & \tau_{1J} & & & \\ & & K_{3\infty} & \tau_{3\infty 3} & & & & \\ & & \tau_{3\infty 3}^{\dagger} & K_3 & \tau_{3J} & & & \\ & \tau_{1J}^{\dagger} & & \tau_{3J}^{\dagger} & K_J & \tau_{2J} & & \tau_{4J} \\ & & & & \tau_{2J}^{\dagger} & K_2 & \tau_{2\infty 2} & \\ & & & & & \tau_{2\infty 2}^{\dagger} & K_{2\infty} & \\ & & & & \tau_{4J}^{\dagger} & & & K_4 \end{bmatrix}$$

$$= \begin{bmatrix} G_{11} & G_{12} & \cdots & G_{18} \\ G_{21} & G_{22} & \cdots & G_{28} \\ \vdots & \vdots & \ddots & \vdots \\ G_{81} & G_{82} & \cdots & G_{88} \end{bmatrix}^{-1} \tag{4}$$

By multiplying to the right with $G^{(r)}$ and identifying block by block within the resulting identity matrix we end up with equation (5), where between the first set of parentheses lie the lines and columns that when multiplied give the rest of identities. Algorithmically, the system of equations translates into:

(1) Build $K_4$. Compute $G_4 = K_4^{-1}$. Compute $\Sigma_4 = \tau_{4J} G_4 \tau_{4J}^{\dagger}$
(2) Build $K_{p\infty}$. Compute $G_{p\infty} = K_{p\infty}^{-1}$. Compute $\Sigma_{p\infty} = \tau_{p\infty p}^{\dagger} G_{p\infty} \tau_{p\infty p}$ ($p = 1$ to 3, for $p = 2$ swap daggers)
(3) Build $K_p$. Compute $G_p = (K_p - \Sigma_{p\infty})^{-1}$. Compute $\Sigma_p = \tau_{pJ}^{\dagger} G_p \tau_{pJ}$
(4) Build $K_J$. Compute $G_J = (K_J - \Sigma_4 - \Sigma_2 - \Sigma_1 - \Sigma_3)^{-1}$
(5) Repeat 1–4. for all energies in the range of interest.

Green's function was calculated using the recurrence relation captured in equation (6), by starting from the identity matrix and iterate to convergence, using two previous steps in a linear mixing scheme.

$$(G_{p\infty})_{1,1} = \left[ (K_{p\infty})_{1,1} - (K_{p\infty})_{1,2\ldots\infty} G_{p\infty} \left( K_{p\infty}^{\dagger} \right)_{2\ldots\infty,1} \right]^{-1}$$

$$= \left[ (K_{p\infty})_{1,1} - (K_{p\infty})_{1,2} (G_{p\infty})_{1,1} \left( K_{p\infty}^{\dagger} \right)_{2,1} \right]^{-1} \tag{6}$$

From the Green's functions of the junction the rest proceeds as usual [25,26], i.e:

(6) Compute coupling $\Gamma_p = i\left(\Sigma_p^{(r)} - \Sigma_p^{(a)}\right)$. Compute transmission $T_{pq} = Tr\left(\Gamma_p G_J^{(r)} \Gamma_q G_J^{(a)}\right)$ (for $p,q = 1\ldots4$)
(7) Compute conductance $\overline{G}_{pq}(E) = (2e^2/h) \int T_{pq}(E') F_T (E - E') \mathrm{d}E'$ with $F_T(E) = (1/4k_B T) \sec h^2 (E/2k_B T)$
(8) Compute loop-current $I_{pq} = (1/e) \int_{\mu_1}^{\mu_2} \overline{G}_{pq}(E) \mathrm{d}E$. Compute lead current $I_p = \sum_q I_{pq}$

$$\begin{cases} (8\times5) \Rightarrow G_{85} = -K_4 \tau_{4J}^{\dagger} G_{55} \equiv -G_4 \tau_{4J}^{\dagger} G_{55} \\ \begin{pmatrix} 1\times5 \\ 2\times5 \end{pmatrix} \Rightarrow G_{25} = -\left(K_1 - \tau_{1\infty 1}^{\dagger} K_{1\infty}^{-1} \tau_{1\infty 1}\right)^{-1} \tau_{1J} G_{55} \equiv -(K_1 - \Sigma_{1\infty})^{-1} \tau_{1J} G_{55} \equiv -G_1 \tau_{1J} G_{55} \\ \begin{pmatrix} 3\times5 \\ 4\times5 \end{pmatrix} \Rightarrow G_{45} = -\left(K_3 - \tau_{3\infty 3}^{\dagger} K_{3\infty}^{-1} \tau_{3\infty 3}\right)^{-1} \tau_{3J} G_{55} \equiv -(K_3 - \Sigma_{3\infty})^{-1} \tau_{3J} G_{55} \equiv -G_3 \tau_{3J} G_{55} \\ \begin{pmatrix} 6\times5 \\ 7\times5 \end{pmatrix} \Rightarrow G_{65} = -\left(K_2 - \tau_{2\infty 2} K_{2\infty}^{-1} \tau_{2\infty 2}^{\dagger}\right)^{-1} \tau_{2J}^{\dagger} G_{55} \equiv -(K_2 - \Sigma_{2\infty})^{-1} \tau_{2J}^{\dagger} G_{55} \equiv -G_2 \tau_{2J}^{\dagger} G_{55} \\ (5\times5) \Rightarrow G_{55} = \left(K_J - \tau_{4J} G_4 \tau_{4J}^{\dagger} - \tau_{2J} G_2 \tau_{2J}^{\dagger} - \tau_{1J}^{\dagger} G_1 \tau_{1J} - \tau_{3J}^{\dagger} G_3 \tau_{3J}\right)^{-1} \equiv (K_J - \Sigma_4 - \Sigma_2 - \Sigma_1 - \Sigma_3)^{-1} \equiv G_J \end{cases} \tag{5}$$

Matrices that have a sub-index $\infty$ are semi-infinite but fortunately for these ones it suffices to compute just the sub-matrix that corresponds to atoms bonded to atoms from adjacent domains. This sub-matrix called the surface

## References


[1] G. de la Torre, W. Blau, T. Torres. A survey on the functionalization of single-walled nanotubes. The chemical attachment of phthalocyanine moieties. *Nanotechnology*, **14**, 765 (2003).
[2] M.J. O'Connell, *et al.* Reversible water-solubilization of single-walled carbon nanotubes by polymer wrapping. *Chem. Phys. Lett.*, **342**, 265 (2001).
[3] M. Zheng, *et al.* Structure-based carbon nanotube sorting by sequence-dependent DNA assembly. *Science*, **302**, 1545 (2003).
[4] C. Rotsch, K. Jacobson, M. Radmacher. Dimensional and mechanical dynamics of active and stable edges in motile fibroblasts investigated by using atomic force microscopy. *Proc. Natl Acad. Sci.*, **96**, 921 (1999).
[5] J. Fritz, M.K. Baller, H.P. Lang, H. Rothuizen, P. Vettiger, E. Meyer, H.-J. Guntherodt, C. Gerber, J.K. Gimzewski. Translating biomolecular recognition into nanomechanics. *Science*, **288**, 316 (2000).
[6] C. Grogan, R. Raiteri, G.M. O'Connor, T.J. Glynn, V. Cunningham, M. Kane, M. Charlton, D. Leech. Characterisation of an antibody coated microcantilever as a potential immuno-based biosensor. *Biosens. Bioelectron.*, **17**, 201 (2002).
[7] P. Poncharal, Z.L. Wang, D. Ugarte, W.A. de Heer. Electrostatic deflections and electromechanical resonances of carbon nanotubes. *Science*, **283**, 15135 (1999).
[8] Y. Arntz, *et al.* Label-free protein assay based on a nanomechanical cantilever array. *Nanotechnology*, **14**, 86 (2003).

[9] H. Dai, J.H. Hafner, A.G. Rinzler, D.T. Colbert, R.E. Smalley. Nanotubes as nanoprobes in scanning probe microscopy. *Nature*, **384**, 147 (1996).
[10] C.L. Cheung, J.H. Hafner, C.M. Lieber. Carbon nanotube atomic force microscopy tips: direct growth by chemical vapor deposition and application to high-resolution imaging. *Proc. Natl Acad. Sci.*, **97**, 3809 (2000).
[11] P. Kim, C.M. Lieber. Nanotube nanotweezers. *Science*, **286**, 2148 (1999).
[12] M. Dequesnes, S.V. Rotkin, N.R. Aluru. Calculation of pull-in voltages for carbon-nanotube-based nanoelectromechanical switches. *Nanotechnology*, **13**, 120 (2003).
[13] L.A. Girifalco, M. Hodak, R.S. Lee. Carbon nanotubes, buckyballs, and a universal graphitic potential. *Phys. Rev. B*, **62**, 13104 (2000).
[14] L. Henrard, E. Hernández, P. Bernier, A. Rubio. van der Waals interaction in nanotube bundles: consequences on vibrational modes. *Phys. Rev. B*, **60**, R8521 (1999).
[15] D. Sánchez-Portal, E. Artacho, J.M. Soler, A. Rubio, P. Ordejón. *Ab initio* structural, elastic, and vibrational properties of carbon nanotubes. *Phys. Rev. B*, **59**, 12678 (1999).
[16] E. Hernández, C. Goze, P. Bernier, A. Rubio. Elastic properties of single-wall nanotubes. *Appl. Phys. A*, **68**, 287 (1999).
[17] T. Belytschko, S.P. Xiao, G.C. Schatz, R.S. Ruoff. Atomistic simulations of nanotube fracture. *Phys. Rev. B*, **65**, 235430 (2002).
[18] W.H. Noon, K.D. Ausman, R.E. Smalley, J.P. Ma. Helical ice-sheets inside carbon nanotubes in the physiological condition. *Chem. Phys. Lett.*, **355**, 445 (2002).
[19] L. Kalé, *et al.* NAMD2: greater scalability for parallel molecular dynamics. *J. Comput. Phys.*, **151**, 283 (1999).
[20] A. MacKerell Jr., *et al.* All-atom empirical potential for molecular modeling and dynamics studies of proteins. *J. Phys. Chem. B*, **102**, 3586 (1998).
[21] T. Werder, J.H. Walther, R. Jaffe, T. Halicioglu, P. Koumoutsakos. Molecular dynamics simulation of contact angles of water droplets in carbon nanotubes. *Nano Lett.*, **1**, 697 (2001).
[22] E.W. Wong, P.E. Sheehan, C.M. Lieber. Nanobeam mechanics: elasticity, strength, and toughness of nanorods and nanotubes. *Science*, **277**, 1971 (1997).
[23] J.M. Soler, *et al.* The Siesta method for *ab initio* order-N materials simulation. *J. Phys.: Condens. Matter*, **14**, 2745 (2002).
[24] Y.G. Yoon, M.S.C. Mazzoni, H.J. Choi, J. Ihm, S.G. Louie. Structural deformation and intertube conductance of crossed carbon nanotube junctions. *Phys. Rev. Lett.*, **86**, 688 (2001).
[25] M.P. Anantram, T.R. Govindan. Conductance of carbon nanotubes with disorder: a numerical study. *Phys. Rev. B*, **58**, 4882 (1998).
[26] S. Datta. *Electronic Transport in Mesoscopic Systems*, Cambridge University Press, Cambridge, UK (1995).
[27] S. Roche, F. Triozon, A. Rubio, D. Mayou. Electronic conduction in multi-walled carbon nanotubes: role of intershell coupling and inconmensurability. *Phys. Lett. A*, **285**, 94 (2001).